Finding a cold needle in a warm haystack: infrared imaging applied to locating cryocooled crystals in loops

Edward H. Snell,[a]* Mark J. van der Woerd,[a] Mitchell D. Miller[b] and Ashley M. Deacon[b]

[a]Biotechnology Science, Code SD46, NASA MSFC, Huntsville, AL 35812, USA, and [b]JCSG/SSRL, Stanford University, 2575 Sand Hill Road, MS 69, Menlo Park, CA 94025, USA. Correspondence e-mail: eddie.snell@msfc.nasa.gov

The use of infrared imaging to locate crystals mounted in cryoloops and cryopreserved in a nitrogen gas stream at 100 K is demonstrated. In the home laboratory, crystals are clearly seen in the infrared images with light transmitting through the sample while irradiating the crystal from behind, and with illumination from a direction perpendicular to the direction of view. The crystals transmit and reflect infrared radiation at different levels to the surrounding mother liquor and loop. Because of differences in contrast between crystals and their surrounding mother liquor, it is possible to identify the crystal position. At the synchrotron, with robotically mounted crystals, the small depth of field of the lens required the recording of multiple images at different focal points. Image processing techniques were then used to construct a clear image of the crystal. The resulting infrared images and intensity profiles show that infrared imaging can be a powerful complement to visual imaging in locating crystals in cryocooled loops.

1. Introduction

Biological crystallography is becoming increasingly automated due to high-throughput structural genomics and structure-based drug discovery efforts (Kuhn et al., 2002; Blundell et al., 2002; Stewart et al., 2002; Stevens et al., 2001; Mittl & Grutter, 2001). Automation of X-ray data collection is one aspect of these efforts (Roth et al., 2002; Muchmore et al., 2000; Abola et al., 2000; Cohen et al., 2002; Snell et al., 2004; Ohana et al., 2004). For effective automation the processes used must be rapid, repeatable and accurate. If we distinguish between preparation and actual data collection during the processing of a crystal on an automated synchrotron beamline, estimates show that over one-half of the time in the sample preparation stage is spent on the alignment of the sample (Abola et al., 2000).

For macromolecular structure determination, crystals are typically mounted in a nylon loop and the system is vitrified in a 100 K nitrogen gas stream (Teng, 1990; Garman, 1999; Garman & Schneider, 1997). Crystal alignment takes place by visually locating the crystal in the loop, and then positioning it at the center of the camera rotation and therefore in the X-ray beam. If the crystal is clearly visible, this process is reliable and rapid. Automated techniques have been developed that make use of image processing algorithms for crystal centering (Karain et al., 2002; Roth et al., 2002; Andrey et al., 2004). However, there are a significant number of cases in which the

crystals cannot be distinguished from the surrounding vitrified liquor and both human and automated techniques fail. In these cases, change of illumination, background or the use of polarized light can help, but these steps add to the time taken to align the sample and are still not always successful.

Visible light is only a small part of the electromagnetic spectrum. The overall spectrum can be divided into two regions, ionizing and non-ionizing, depending on the wavelength (or energy) of the radiation. Ionizing radiation, e.g. X-ray or ultraviolet, can break chemical bonds and, therefore, damage macromolecules. Visible light is non-ionizing and does not break chemical bonds, making it the preferred method for non-invasive crystal observation. Another non-ionizing part of the spectrum is infrared radiation. This is absorbed by most atmospheric components, including nitrogen, water, oxygen and carbon dioxide. However, there are several windows in which the atmosphere is transparent to infrared radiation. These windows are termed near, mid and far infrared. We have made use of the mid-infrared window to image the macromolecular cryocooling process (Snell et al., 2002). This study showed that the crystals could clearly be distinguished from the loop and mother liquor even after the system had reached thermal equilibrium. In this paper we have explored this property and applied it, both in the home laboratory setting and on a high-throughput synchrotron beamline, to locate crystals in loops that were difficult to locate with visual-light methods. To date, there is no completely successful

automated system to align the crystal in the X-ray beam. A system that can accomplish this opens the way to completely automated data collection.

2. Laboratory-based studies

2.1. Instrumentation

The infrared camera used was an Indigo Systems Phoenix infrared camera cooled by an internal liquid-nitrogen Dewar. In the laboratory it was positioned to image the center of a Hampton Research cryoloop. The loop was mounted on a goniometer head with a rotatable φ axis. On the opposite side of the loop a long-working-distance NAVITAR optical telescope lens with a COHU CCD camera also imaged the center of the loop. This setup allowed for simultaneous sample observation with infrared and visible light (Fig. 1). The entire system (excluding the infrared camera) was mounted on an optical table. An Oxford 600 cryostream operating at 100 K was used to cool the loop. The loop was illuminated at an angle of approximately $45°$ with the optical axis, using an incandescent lamp, thus providing both visible light and infrared illumination. The infrared camera was mounted on a tripod with manual positioning adjustment. The Phoenix camera uses an indium antimonide (InSb) type detector with 320×256 pixels in a 30 mm^2 area and a spectral range of 1.5–5.0 µm. A 3.0–5.0 µm bandpass filter limits the wavelength to the mid-infrared window. The camera was equipped with a $4\times$ magnification Si:Ge infrared lens.

Individual infrared detectors, or pixels, vary in their response to thermal energy. To overcome this non-uniformity, a correction has to be applied for each exposure time that will be used. This non-uniformity correction is achieved by imaging two objects of uniform temperature, one at the high-temperature limit of the observation range and the other at the low limit. In our previous work (Snell et al., 2002), we used an infrared camera to look at the cryocooling of crystals and used two black metal plate sources at 293 and 193 K for non-uniformity correction. In the work described here, we used the same high-temperature object, but the cold source was a steel block, $305 \times 200 \times 200$ mm, with a 75 mm diameter, 180 mm deep, cylindrical hole drilled into it. The camera lens is partially inserted into this hole to ensure a completely uniform temperature reading, while the behavior of the hole is close to that of a black-body. The block is instrumented with internal and external thermocouples and cooled by liquid nitrogen. The block is cooled to below the required source temperature, allowed to come to equilibrium and then to warm up to the required temperature. To determine the camera sensitivity, images were recorded over time as the block warmed up, starting at 80 K. For each image, the camera was focused on the hole in the block, an image recorded, then the camera removed from the vicinity of the cold block to prevent cooling of the lens. The minimum temperature at which the camera is sensitive, defined as the point where a signal was seen above the electronic noise, was determined to be approximately 135 K. In a subsequent experiment, the block was cooled and then allowed to warm up gradually, and images of the hole in the block were recorded with exposure times of 1.0, 2.5, 5.0 and 10.0 ms at a temperature of 193 K. At this temperature, the warming rate of the block has slowed down far enough that it remains stable over a time period enabling successive measurements at the same temperature. Images were also recorded at a corresponding exposure times of a black plate at 293 K. A non-uniformity correction function was calculated from these measurements for each exposure time and stored in the camera memory.

2.2. Samples

The three crystal systems used were lysozyme, a recombinant xylose isomerase and a basic fibroblast growth factor DNA complex. The lysozyme crystals were grown in the presence of $20\%(v/v)$ ethylene glycol, the xylose isomerase crystals were grown in the presence of $8\%(v/v)$ ethylene glycol and the bFGF/DNA complex was cryoprotected by soaking the crystals in mother liquor to which $25\%(v/v)$ 2,3-butanediol was added. The cryoprotectant conditions for all the systems had been previously optimized for the best X-ray diffraction data. The lysozyme crystals are in space group $P4_32_12$, with cell parameters $a = b = 78.5$, $c = 37.8$ Å, the bFGF/DNA complex crystals are in space group $P622$, with $a = b = 112.8$, $c = 450.2$ Å, and the xylose isomerase crystals are in $I222$, with $a = 92.5$, $b = 98.2$, $c = 102.2$ Å.

2.3. Experimental

The crystals were mounted directly from their growth solution using a Hampton Research cryoloop of 0.5 mm horizontal width. The same loop was used for each crystal and was washed with water, then ethanol, and subsequently dried between samples. Small thin crystals were deliberately chosen to represent the most difficult cases for crystal observation and alignment. For each crystal, a visual image of the
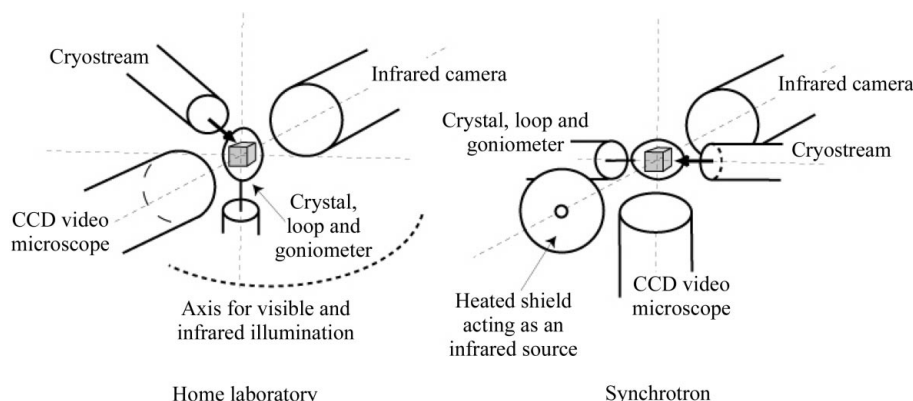

Figure 1
Schematic drawing showing the experimental setup for the laboratory and synchrotron measurements (not to scale). The synchrotron setup is shown in detail in Fig. 2.

crystal in the loop was recorded using the CCD video camera and the visual-light telescope objective. These visual images were optimized as a function of lighting position and choice of background to provide the best image of the crystal with the instrumentation available and to serve as a reference for the infrared imaging.

Lysozyme (0.14 × 0.11 × 0.06 mm), bFGF/DNA complex (0.11 × 0.17 × 0.05 mm) and xylose isomerase crystals (0.08 × 0.08 × 0.04 mm) were cryocooled by blocking the cryostream, placing the loop holding the crystal on the goniometer and then unblocking the cryostream. The crystals were imaged at 100 K with the loop perpendicular to the direction of observation and illuminated from the side after several minutes of cooling. To determine the angular sensitivity of the technique a cryocooled bFGF/DNA complex crystal was imaged perpendicular to the camera and then at 45° φ intervals from −90 to +90° from the original position. In each case, the infrared camera and crystal position (x, y and z goniometer translation) was adjusted until the optimum visual and infrared image was seen.

To determine whether transmission of infrared light through the sample or reflection of infrared light off the sample surface gave the best image quality with sufficient contrast to distinguish the crystal from its environment, the light source was moved from illuminating the side of the crystal to illuminating the rear, directly behind the loop. Xylose isomerase was cryocooled and then imaged with successive exposure times of 1.0, 2.5, 5.0 and 10.0 ms.

2.4. Image analysis

The images were analyzed using *Talon* (Indigo Systems Corporation), a modified version of *ImagePro Plus*, and the intensity profiles of lines passing through the images were produced. The images were displayed on a gray scale with white representing warm (high intensity) and black cold (low intensity).

3. Synchrotron-based studies

3.1. Instrumentation

Following the laboratory experiments, the same camera was mounted on beamline 11-1 of the Stanford Synchrotron Radiation Laboratory (SSRL). The camera was mounted in an orientation different from that used in the laboratory studies so that it imaged down the beam path perpendicular to the rotation axis of the crystal (Figs. 1 and 2). The camera is cooled by liquid nitrogen and operates horizontally because of the liquid-nitrogen Dewar limitations. In an actual application, the camera can be replaced with one that operates in a vertical position so that it does not impede the beam. The camera was mounted to optical rails attached to the experimental table in the position in which the detector is normally located. This setup allowed accurate x, y and z positioning (in comparison with the manual positioning for the laboratory case). To provide image contrast, a heated shield, normally used to prevent ice formation on the goniometer head, was placed on
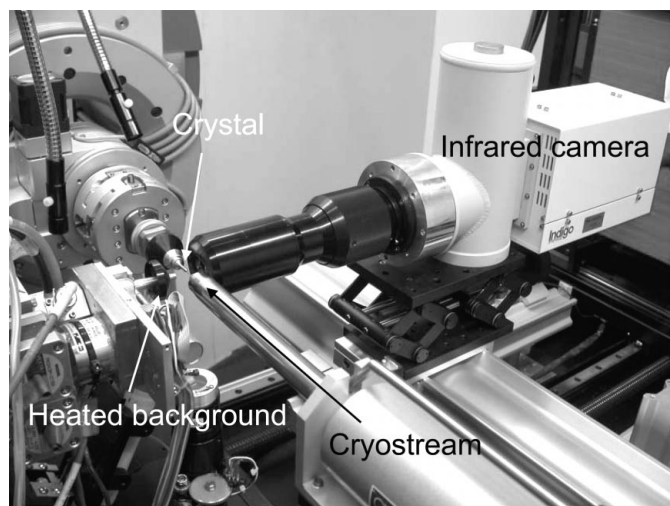
Figure 2
Photograph of the experimental setup on Stanford Synchrotron Radiation Laboratories beamline 11-1.

Lysozyme in visible light — Infrared
(a)

bFGF/DNA in visible light — Infrared
(b)

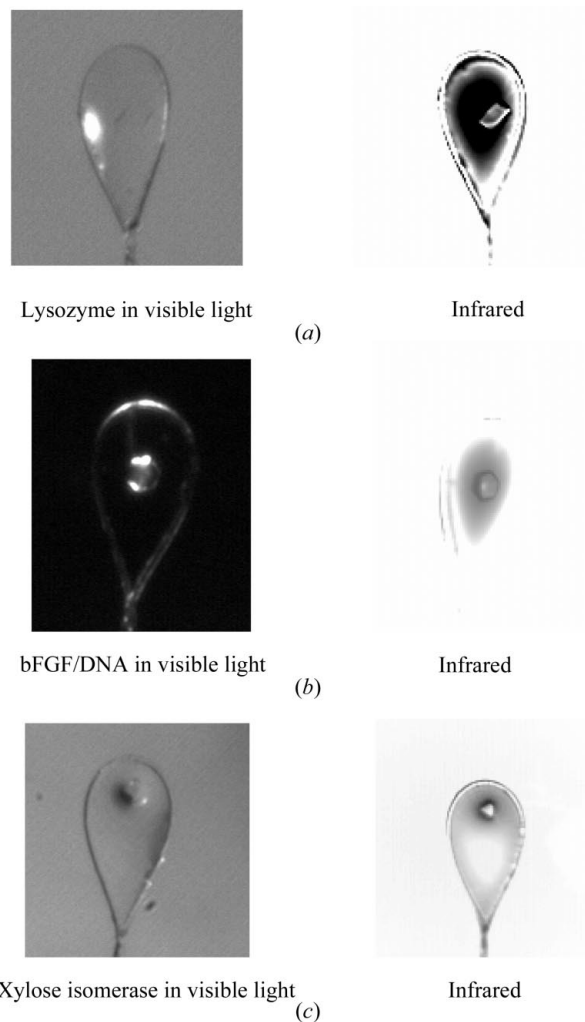Xylose isomerase in visible light — Infrared
(c)

Figure 3
Visible and infrared images of crystals of lysozyme, bFGF/DNA complex and xylose isomerase cryocooled at 100 K. For scale, the loop in each image is 0.5 mm across, the lysozyme crystal measures 0.14 × 0.11 × 0.06 mm, the bFGF/DNA complex crystal 0.11 × 0.17 × 0.05 mm and the xylose isomerase crystal 0.08 × 0.08 × 0.04 mm.

the beamline collimator behind the crystal position. This shield was heated in pulses to 323 K. An automated crystal mounting system (Cohen *et al.*, 2002), developed by the Joint Center for Structural Genomics (JCSG; http://www.jcsg.org) and the SSRL structural molecular biology group, was used for mounting samples.

3.2. Samples

The samples were part of the Tier I shotgun crystallization screen of the *Thermotoga maritima* proteome (Lesley *et al.*, 2002). Crystals were produced directly from a course crystallization screen using 50 + 50 nl sitting drops, harvested, flash cooled in liquid nitrogen and stored in an SSRL-style sample cassette (Cohen *et al.*, 2002). 12 crystals from nine targets were selected and imaged with both infrared and visible light on beamline 11-1. The sample crystals had varying morphology. Crystal size ranged from 10 to 200 µm, with most having the longest dimension between 75 and 125 µm. Some of the samples had ice build-up on the surface of the loop.

3.3. Experimental

Tests quickly revealed that the depth of field of the lens was a significant limiting factor. A modified experimental procedure was adopted to overcome this problem with the instrumentation available. A pre-cooled xylose isomerase crystal similar to that used in the laboratory studies was mounted to test the new protocol, which involved collecting a series of images from each sample. The sample was translated in the horizontal axis along the path of the X-ray beam until the best image of the loop was seen. Next, the sample was translated away from the camera until the loop image was out of focus. Images were then recorded at 10 µm translation intervals from this point back toward the camera and subsequently passing through the sample focal plane until the image of the loop was again out of focus. This procedure resulted in 20–30 images for each loop. In the time available, a total of five crystals were then imaged using this modified experimental protocol.

3.4. Image processing

The images taken at successive depths of field were processed using *ImagePro Plus* and the *SharpStack* module available for the software. *SharpStack* takes a succession of images at different focal points through the object and attempts to produce a single focused image from them. Four different image processing approaches were evaluated to extract an image of the crystal from the data: extended depth of field construction, blind deconvolution and two deblurring techniques (Wallace *et al.*, 2001). Extended depth of field processing makes use of the fact that each image is a focal volume, the depth of the volume being equal to the depth of focus. Any surface that intersects this volume will appear as a sharp image. Sharp areas in each focal volume are identified and integrated into a composite image. Blind deconvolution determines a point spread function for the blur imposed by the optical system and deconvolves that function from the images (Holmes *et al.*, 1995). The two deblurring techniques were no-neighbor (Monck *et al.*, 1992) and nearest-neighbor deblurring (Agard, 1984). Processing took place almost instantaneously on a 1.4 GHz Pentium processor personal computer.
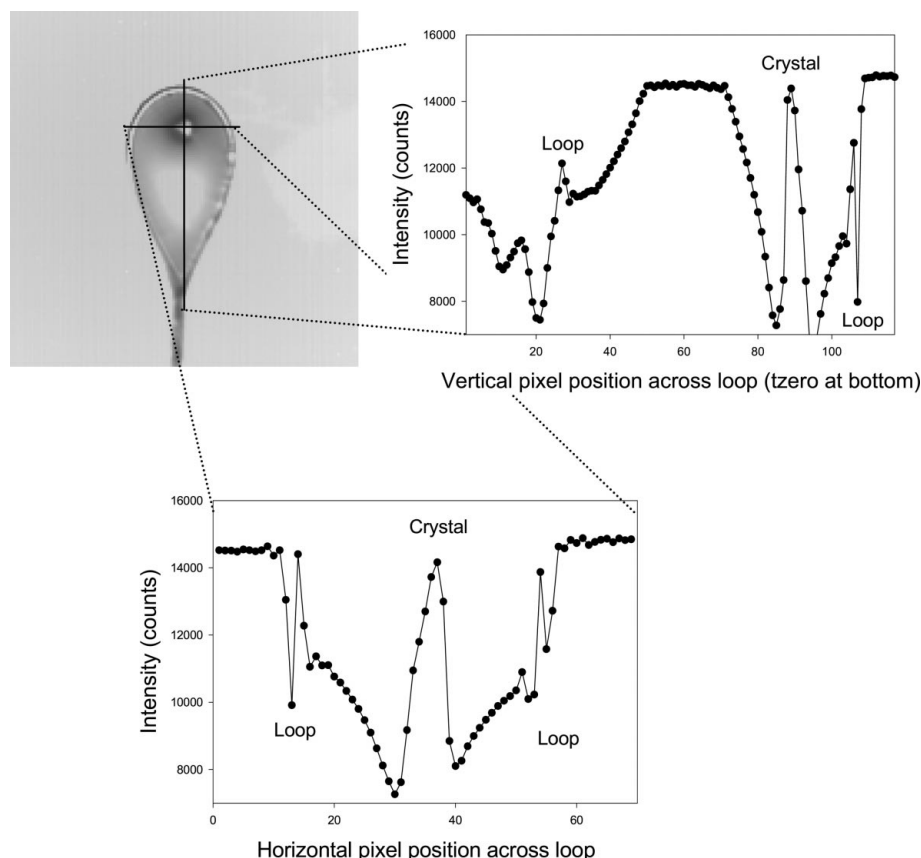
4. Results

4.1. Laboratory case

The images recorded are shown in Fig. 3. Visible-light images of a lysozyme crystal, a bFGF/DNA complex crystal and a xylose isomerase crystal are shown. The illumination angle and background (or lack of it) were optimized to obtain the best possible visible image. To the right of the visible-light image is the corresponding infrared image. To facilitate comparison, the infrared images are shown in the same orientation as the images recorded by visible light, *i.e.* as a

Figure 4
Plot of the intensity profiles recorded vertically and horizontally across the infrared image of the xylose isomerase crystal illustrated in Fig. 3(*c*).

mirror image of that recorded. As a result of the setup, the infrared camera is imaging the reverse side of the loop compared with the visible-light CCD camera. In each infrared image, the crystal is clearly visible. The bFGF/DNA complex crystal and xylose isomerase crystal are also visible in the visual CCD, but the lysozyme crystal is hard to distinguish from the surrounding vitrified liquid.

Fig. 4 shows the infrared intensity profile plotted across the vertical and horizontal positions of the xylose isomerase crystal also illustrated in Fig. 3(c). The intensity is directly related to the amount of infrared radiation received by the detector face; the higher the intensity, the more infrared radiation is received by the camera. In this image, the crystal appears as a bright peak surrounded by dark valleys corresponding to an object reflecting or transmitting more infrared radiation than its immediate vitrified environment. Further from the crystal is a bright plateau corresponding to a warm background. The loop itself appears as bright peaks in the

intensity profile. Note that while the crystal has reached equilibrium and remains at 100 K, the image contrast is produced by the transmission or reflection of external thermal radiation and the thermal properties of the system, *i.e.* the cryocooled crystal, loop and liquid, under study.

In Fig. 5(a), the bFGF/DNA complex crystal is shown using visible-light imaging. It is also shown in the infrared at φ angles of 0, 45, 90, −45 and −90°. The crystal is clearly visible from −45 to 45° in φ (Figs. 5b–5c) but not immediately obvious at angles of ±90° (Figs. 5d and 5f).

When the crystal is illuminated from behind it is clearly visible. Fig. 6 shows an example of a xylose isomerase crystal imaged visually with a white background (Fig. 6a) and without a background (Fig. 6b). The same crystal is shown in infrared images at successive exposure times of 1.0, 2.5, 5.0 and 10 ms (Figs. 6c–6f). The crystal is clearly seen as a dark region in the infrared image. For each panel in Figs. 6(c)–6(f), the gray scale
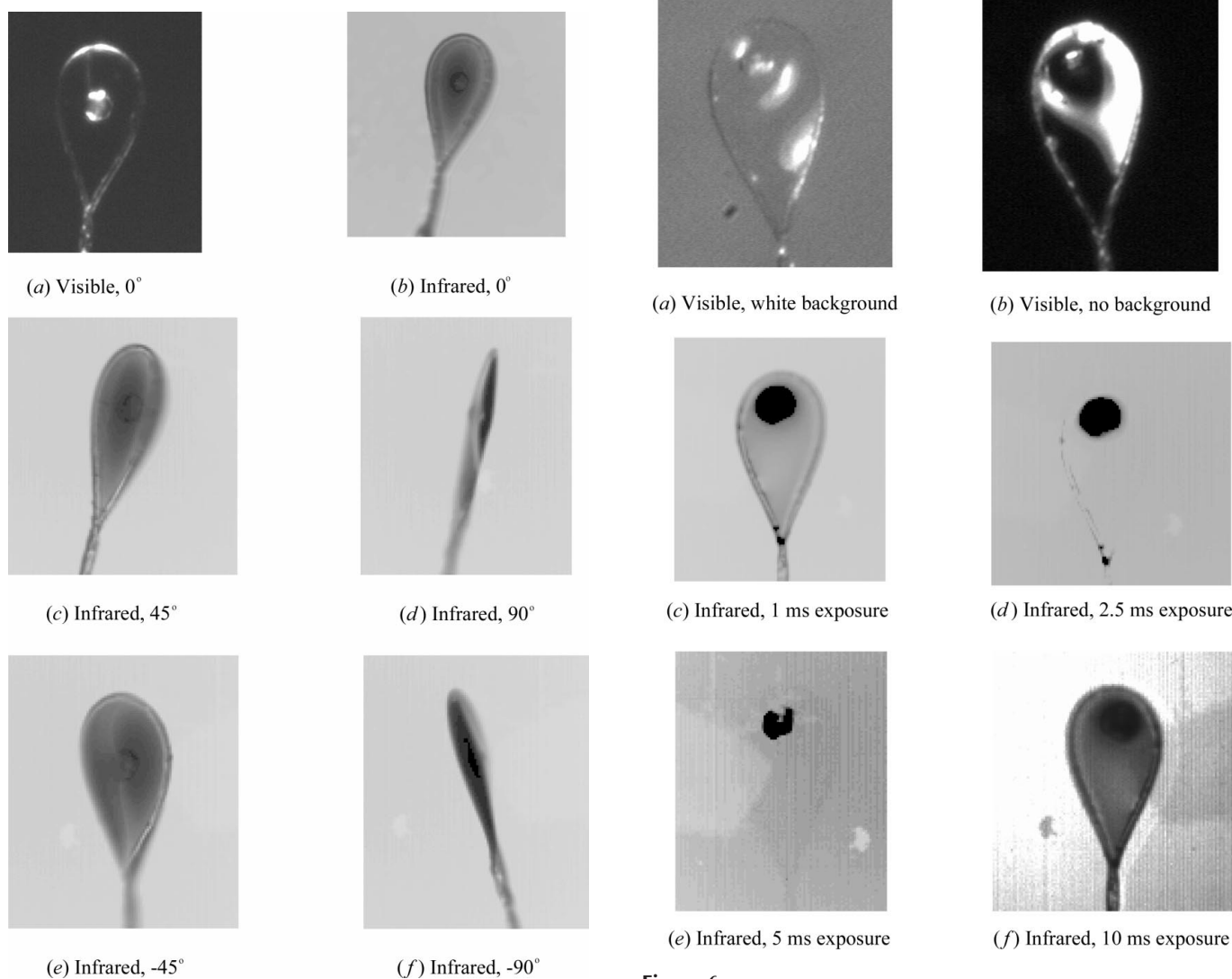

(a) Visible, 0°

(b) Infrared, 0°

(c) Infrared, 45°

(d) Infrared, 90°

(e) Infrared, -45°

(f) Infrared, -90°

Figure 5
Visible image of a bFGF/DNA complex crystal shown with infrared images at 0, 45, 90, −45 and −90° in φ. For scale, the loop is 0.5 mm across its widest point.

(a) Visible, white background

(b) Visible, no background

(c) Infrared, 1 ms exposure

(d) Infrared, 2.5 ms exposure

(e) Infrared, 5 ms exposure

(f) Infrared, 10 ms exposure

Figure 6
Images of a xylose isomerase crystal using visible light (a) with and (b) without a white background. Infrared images of the same crystal recorded at exposure times of 1.0, 2.5, 5.0 and 10 ms are shown in panels (c) through (f). For scale, the loop is 0.5 mm across at its widest point.

has been adjusted to optimize the visibility of the crystal. In Fig. 7, the infrared intensity is plotted across the loop for each of the recorded exposure times. For exposure times up to 5 ms the crystal appears as a dark object in the otherwise bright image. At 10 ms exposure time, on the intensity scale shown, it is difficult to discern the crystal position. The most sensitive imaging occurs at the shortest exposure time used. As the exposure time is reduced, more detail becomes apparent in the intensity profile.

4.2. Synchrotron case

A xylose isomerase crystal mounted robotically at the synchrotron beamline is shown in Fig. 8. The best focused image from the sequence of successive images at focal points through the loop is shown in Fig. 8(a). Images generated from image processing by the application of the no-neighbor algorithm, the nearest-neighbor algorithm and an inverse filter deconvolution are shown in Figs. 8(b)–8(d), respectively. The extended depth of field processing did not produce an image that was improved over the original. The infrared intensity *versus* pixel position for the inverse filter and nearest-neighbor algorithms, the two best crystal signatures, are shown in Figs. 9 and 10. The infrared signal seen from the crystal is not as pronounced as the laboratory test cases, but the crystal is still located.

Sample crystals from the Joint Center for Structural Genomics are shown in Fig. 11. Visually, crystal 1 is a 0.12 × 0.04 × 0.02 mm rectangular prism and crystal 2 is a 0.23 × 0.01 × 0.01 mm needle. Crystal 3 is a 0.11 × 0.11 × 0.01 mm hexagonal plate and crystal 4 is a 0.11 × 0.08 × 0.08 mm needle. Crystal 5 consists of two objects, a 0.11 × 0.04 × 0.04 mm plate at the base of the loop and a 0.12 × 0.10 × 0.05 mm cracked crystal. For crystals 1 and 5, 30 and 15% glycerol was used as a cryoprotectant, respectively. For crystals 2–4, 20% PEG 3350 was used in each case. In the infrared, each crystal is seen with the artificial depth of field created from image processing of successive images. The contrast is not as high as that seen in the laboratory, but the results are a strong indicator of the potential of the technique.

5. Discussion

In the laboratory experiment, we are able to see the crystals clearly in the infrared. The intensity profile has a well defined shape, which makes it easy to identify the loop and the crystal (see Fig. 4). The crystal is still visible at φ angles of −45 and +45° away from directly facing the camera
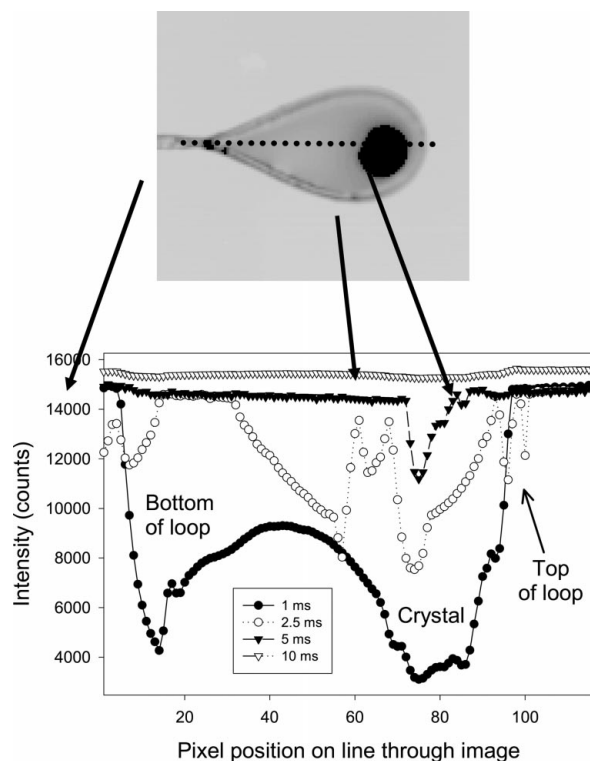

Figure 7
The intensity cross section of the images in Fig. 6 (exposure times of 1.0, 2.5, 5.0 and 10.0 ms) from the loop base to the tip. For illustrative purposes, the xylose isomerase crystal imaged at 1 ms exposure time is shown to relate the intensity profile to the sample.
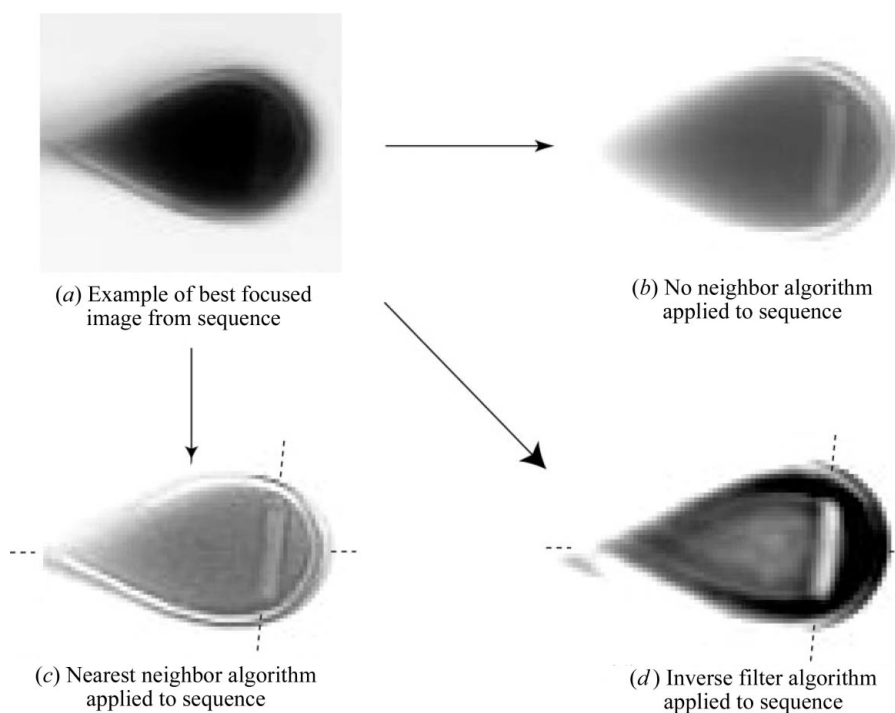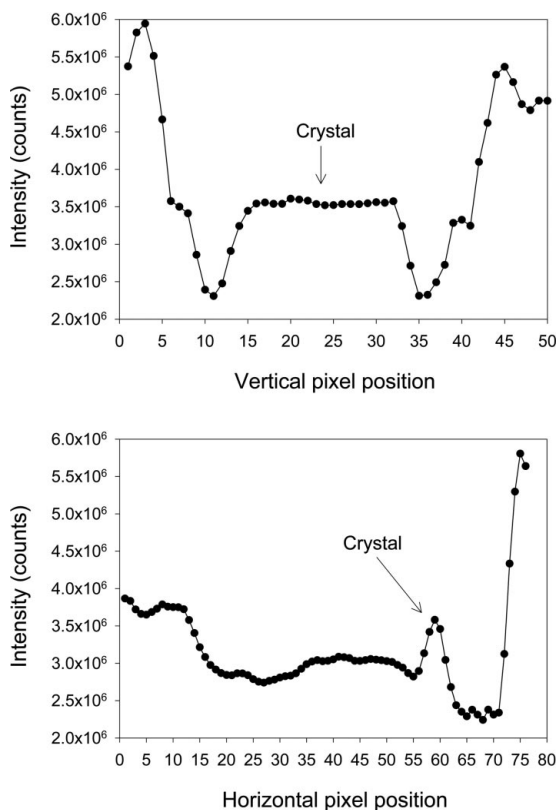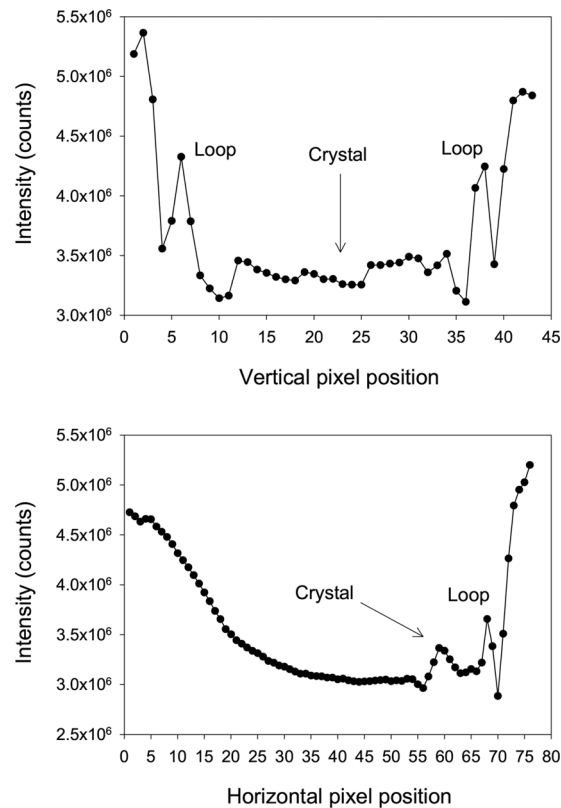

(a) Example of best focused image from sequence

(b) No neighbor algorithm applied to sequence

(c) Nearest neighbor algorithm applied to sequence

(d) Inverse filter algorithm applied to sequence

Figure 8
Infrared images of a mounted xylose isomerase crystal showing the best single image from (a) the sequence of focal points, (b) the sequence with a no-neighbor algorithm applied, (c) the sequence with a nearest-neighbor algorithm applied and (d) the sequence with an inverse filter algorithm applied.

Figure 9
Plot of intensity against pixel position along the dotted lines shown in Fig. 8 for the best focused image produced by the inverse filter algorithm. In each case, the xylose isomerase crystal position is indicated.

Figure 10
Plot of intensity against pixel position along the dotted lines shown in Fig. 8 for the best focused image produced by the nearest-neighbor algorithm. In each case, the xylose isomerase crystal position is indicated along with the intensity due to the loop.

(see Fig. 5). Exposure time is also an important factor in the imaging (Figs. 6 and 7). If the exposure time is too short, the crystal is not visible; if it is too large, there is a risk of overload and the crystal is masked out by noise. In our experiments, the best exposure time to provide a clear signal for the crystal is between 2.5 and 5 ms. An exposure of 1 ms starts to blur the boundary between the loop and the crystal. For exposure times beyond 5 ms, the signal is reduced and the crystal image is lost in noise. Non-uniformity corrections are pre-stored in the camera memory for each planned exposure time. During the experiment it is not possible to perform additional non-uniformity corrections and consequently exposure times are limited to those that are pre-defined.

We are imaging the crystal, loop and vitrified liquid at thermal equilibrium at 100 K. According to Planck's law, all objects emit radiation as a function of their temperature. For a perfect emitter and absorber (a black-body) this energy spectrum can be calculated as a function of temperature. In practice, objects such as crystals in loops and the loops themselves are not ideal black-bodies, *i.e.* they do not perfectly absorb or emit thermal radiation. The infrared camera is only sensitive to temperatures above ~135 K. Unlike the previous study using infrared imaging to look at cryocooling (Snell *et al.*, 2002), we are not measuring a temperature change but are taking advantage of the non-ideality of our system. In the cases studied, the crystal, loop and vitrified liquid are at the same temperature, but show different infrared transmission

and reflection properties. This difference produces contrast, allowing samples to be seen.

The laboratory experiments were performed by focusing the camera on each individual crystal in a loop positioned perpendicular to the lens, because the depth of field of the lens used for these studies is small, of the order of 10 μm. At the synchrotron, SSRL beamline 11-1, the camera was fixed to a translation stage and the loops with crystals were robotically mounted on the goniometer (Cohen *et al.*, 2002). The loops were automatically centered in the X-ray beam (Miller *et al.*, 2004) and positioned such that they were as perpendicular to the infrared lens as the single axis of the goniometer allowed. Care was taken to mount crystals in loops slightly larger than the maximum dimension of the crystal. This minimizes the need to center the crystal actively, but is not an optimal solution as the crystal may not be positioned in the center of the loop. It is possible to optimize the position by manual intervention, based on a video microscope image. The crystals mounted on the beamline are a more realistic case to study as the loop and camera position are more precisely controlled. To overcome the small depth of field, successive images at different focal points were collected, and subsequent image processing was used to produce one focused image. The lens was designed for 4× magnification studies at short working distances, which is not optimal for use in observing cryocooled crystals. Lenses can be produced with increased magnification
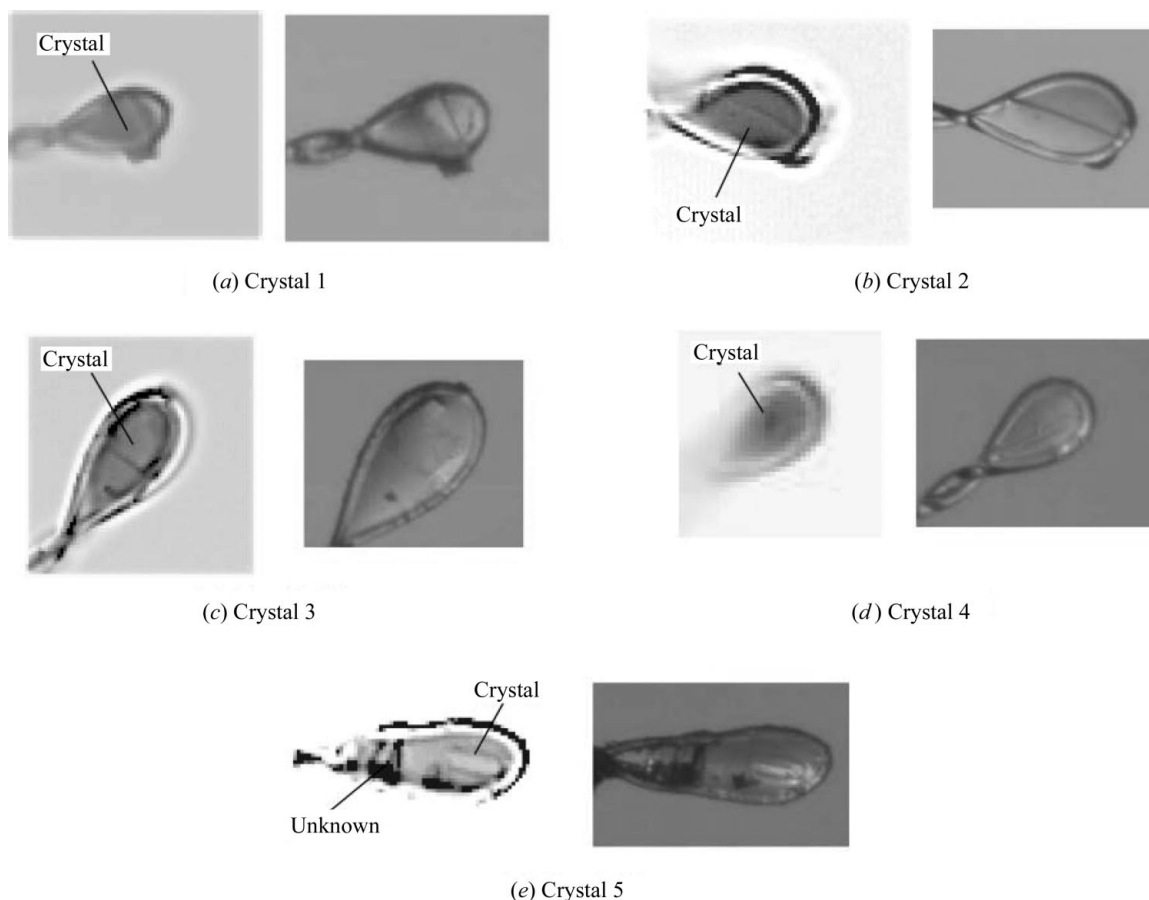
(a) Crystal 1

(b) Crystal 2

(c) Crystal 3

(d) Crystal 4

(e) Crystal 5

Figure 11
Example images of robotically mounted crystals from the Joint Center for Structural Genomics. For each image, the infrared image is shown on the left with the visible image on the right. Images have been scaled to be approximately similar in magnification. The visual and infrared images were recorded in approximately the same position. Note that the infrared images are presented on a 14 bit gray scale and detail is lost in this reproduction.

and/or depth of field but are non-standard and have to be specially made. We did not have one of these available to us for these studies, but our preliminary results demonstrate the potential of the technique. In both cases, the laboratory and at the synchrotron, we have not optimized the surroundings for infrared observations. No shielding is in place against stray thermal radiation and the thermal sources used for illumination were non-uniform. We expect that the technique here demonstrated can be improved by using a lens with an increased depth of field and by optimization of the illumination system.

6. Conclusion

In the laboratory, infrared imaging is very successful at locating crystals within cryoloops and vitrified mother liquor. Under a more realistic high-throughput setting with both mounting technology and crystal samples from the JCSG project, we have demonstrated the application of this technique with a limited number of diverse macromolecular crystalline samples. The method can be improved significantly by using a custom lens, optimized background illumination and shielding of stray illumination. Testing of these improvements with a wider selection of crystals and cryoprotectants,

and a variety of icing and visibility problems, will be needed to demonstrate completely the utility of the method. However, the preliminary results shown here demonstrate that infrared imaging in combination with visible imaging has a potential to improve the success of automated crystal centering in the beam.

References

Abola, E., Kuhn, P., Earnest, T. & Stevens, R. C. (2000). *Nat. Struct. Biol.* **7**(Suppl.), 973–977.

Agard, D. (1984). *Annu. Rev. Biophys. Bioeng.* **13**, 191–219.

Andrey, P., Lavault, B., Cipriani, F. & Maurin, Y. (2004). *J. Appl. Cryst.* **37**, 265–269.

Blundell, T. L., Jhoti, H. & Abell, C. (2002). *Nat. Rev. Drug Discov.* **1**, 45–54.

Cohen, A. E., Ellis, P. J., Miller, M. D., Deacon, A. M. & Phizackerley, R. P. (2002). *J. Appl. Cryst.* **35**, 720–726.

Garman, E. (1999). *Acta Cryst.* D**55**, 1641–1653.

Garman, E. F. & Schneider, T. R. (1997). *J. Appl. Cryst.* **30**, 211–237.

Holmes, T. J., Bhattacharyya, S., Cooper, J. A., Hanzel, D., Krishnamurthi, V., Lin, W., Roysam, B., Szarowski, D. H. & Turner, J. N. (1995). *Light Microscopic Images Reconstructed by Maximum Likelihood Deconvolution*, *Handbook of Biological Confocal Microscopy*, edited by J. B. Pawley, pp. 389–402. New York: Plenum.

Karain, W. I., Bourenkov, G. P., Blume, H. & Bartunik, H. D. (2002). *Acta Cryst.* D**58**, 1519–1522.

Kuhn, P., Wilson, K., Patch, M. G. & Stevens, R. C. (2002). *Curr. Opin. Chem. Biol.* **6**, 704–710.

Lesley, S. A., Kuhn, P., Godzik, A., Deacon, A. M., Matthews, I., Kreusch, A., Spraggon, G., Klock, H. E., McMullan, D., Shin, T., Vincent, J., Robb, A., Brinen, L. S., Miller, M. D., McPhillips, T. M., Miller, M. A., Scheibe, D., Canaves, J. M., Guda, C., Jaroszewski, L., Shelby, T. L., Elsliger, M. A., Wooley, J., Taylor, S. S., Hodgson, K. O., Wilson, I. A., Schultz, P. G. & Stevens, R. C. (2002). *Proc. Natl Acad. Sci. USA*, **99**, 11664–11669.

Miller, M. D., Brinen, L. S., Cohen, A., Deacon, A. M., Ellis, P., McPhillips, S. E., McPhillips, T. M., Phizackerley, R. P., Soltis, S. M., van den Bedam, H., Wolf, G., Xu, Q. & Zhang, Z. (2004). *Proceedings of Synchrotron Radiation Instrumentation: Eighth International Conference on Synchrotron Radiation Instrumentation – SRI2003, San Francisco, August 2003*, pp. 1233–1236. AIP.

Mittl, P. R. & Grutter, M. G. (2001). *Curr. Opin. Chem. Biol.* **5**, 402–408.

Monck, J. R., Oberhauser, A. F., Keating, T. J. & Fernandez, J. M. (1992). *J. Cell Biol.* **116**, 745–759.

Muchmore, S. W., Olson, J., Jones, R., Pan, J., Blum, M., Greer, J., Merrick, S. M., Magdalinos, P. & Nienaber, V. L. (2000). *Struct. Fold. Des.* **8**, R243–246.

Ohana, J., Jacquamet, L., Joly, J., Bertoni, A., Taunier, P., Michel, L., Charrault, P., Pirocchi, M., Carpentier, P., Borel, F., Kahn, R. & Ferrer, J. L. (2004). *J. Appl. Cryst.* **37**, 72–77.

Roth, M., Carpentier, P., Kaikati, O., Joly, J., Charrault, P., Pirocchi, M., Kahn, R., Fanchon, E., Jacquamet, L., Borel, F., Bertoni, A., Israel-Gouy, P. & Ferrer, J. L. (2002). *Acta Cryst.* D**58**, 805–814.

Snell, E. H., Judge, R. A., Larson, M. & van der Woerd, M. J. (2002). *J. Synchrotron Rad.* **9**, 361–367.

Snell, G., Cork, C., Nordmeyer, R., Cornell, E., Meigs, G., Yegian, D., Jaklevic, J., Jin, J., Stevens, R. C. & Earnest, T. (2004). *Structure (Camb.)*, **12**, 537–545.

Stevens, R. C., Yokoyama, S. & Wilson, I. A. (2001). *Science*, **294**, 89–92.

Stewart, L., Clark, R. & Behnke, C. (2002). *Drug Discov. Today*, **7**, 187–196.

Teng, T. Y. (1990). *J. Appl. Cryst.* **23**, 387–391.

Wallace, W., Schaefer, L. H. & Swedlow, J. R. (2001). *BioTechniques*, **31**, 1076–1097.